

## Sensitivity of the Mediterranean circulation to horizontal space-time-dependent tracer diffusivity field in a OGCM

V. RUPOLO<sup>(1)(\*)</sup>, A. BABIANO<sup>(2)</sup>, V. ARTALE<sup>(1)</sup> and D. IUDICONE<sup>(3)</sup>

<sup>(1)</sup> *ENEA - Rome, Italy*

<sup>(2)</sup> *LMD-ENS - Paris, France*

<sup>(3)</sup> *IFA-CNR - Rome, Italy*

(ricevuto il 2 Dicembre 2002; revisionato il 27 Giugno 2003; approvato il 10 Luglio 2003)

**Summary.** — The sensitivity of the Mediterranean circulation to the variability of the horizontal mixing is investigated using a Bryan-Cox-type general circulation model (OGCM). Attention is focused on a parameterisation of mixing previously developed in the context of two-dimensional turbulence, that is for the first time implemented in a OGCM. This parameterisation is suitable for velocity fields characterised by the presence of geostrophic coherent structures, and it is a direct application of the well-known Taylor's dispersion relation. Theoretical and experimental justifications of the parameterisation are discussed and results from four numerical experiments, with different tracer mixing schemes, are presented. In particular, it is shown that the proposed diffusivity parameterisation improves the tracers transport due to large eddy dynamics and, ensuring a more correct salt budget in the north western part of the basin, contributes to maintain a realistic vertical stratification and winter deep convection in long climatic integrations.

PACS 92.10.Lq – Turbulence and diffusion.

PACS 92.10.Mr – Thermohaline structure and circulation.

PACS 92.10.Ty – Fronts and jets.

PACS 93.30.Rp – Regional seas.

### 1. – Introduction

Ocean dynamics is inhomogeneous, both in the steady and in the residual part of motion and present numerical simulations of the general circulation reproduce this inhomogeneity even if the eddy component, that strongly affects tracer transport properties, is not fully resolved. When diffusion processes are not spatially homogeneous, tracers are advected by the “Lagrangian mean velocity”  $\tilde{\underline{u}} = \underline{u} - \nabla K$  [1, 2], where  $K$  is the space-dependent diffusivity field. The extra term  $-\nabla K$  can substantially modify the tracers

---

(\*) E-mail: [volfango.rupolo@casaccia.enea.it](mailto:volfango.rupolo@casaccia.enea.it)

distribution; for instance Armi [3] and Armi and Haidvogel [4], using steady-state advective diffusive model, have shown that tongue-like distributions, such that of the salty Mediterranean outflow in the North Atlantic, can be generated by a purely diffusive field with variable and/or anisotropic diffusion.

Mesoscale eddies move nearly parallel to isopycnal surfaces and are mainly produced by baroclinic instabilities. These two simple observations inspired in the last years the main improvements in the diffusivity parameterisations (for a review see [5-7]).

In this paper we study the influence of horizontal kinematic inhomogeneities on the diffusivity parameterisation. In fact, even if baroclinic instability is an important mechanism of energy extraction, the scenario in which the source of eddy energy is the mean kinetic, rather than the available potential, energy cannot be totally neglected. For instance, McWilliams and Gent [8] proposed diffusivity to be proportional to the local kinetic energy times a tapering time-dimensional factor, with prescribed spatial form, to avoid an overestimate of diffusivity in the energetic border currents.

Moreover, Larichev and Held [9] noted that the extraction of energy from the background flow is dominated by the largest eddy excited by the barotropic quasi-2D inverse cascade and not by the deformation radius. In this barotropization of the flow, local and baroclinic parameterisations cannot represent the non-local effects of large eddy dynamics on the mixing properties.

The purpose of this work is to document this last point by implementing in a OGCM a diffusivity parameterisation that takes into account the *non-local* character of *horizontal* kinematic inhomogeneities of the velocity field. In this parameterization, that was originally proposed by Babiano *et al.* (see [10], hereafter referred as BBRs), the eddy coefficient is proportional to the eddy kinetic energy and inversely proportional to the square root of enstrophy. BBRs introduced their parameterisation in the context of a two-dimensional turbulent flow containing sporadic coherent vortices. In an oceanic context, this corresponds to focus the interest on large-scale flows characterised by the presence of geostrophic 2D coherent structures. Our approach can be considered as complementary to the more usual one of searching to extrapolate to the grid size unresolved effects of baroclinic instability and it is clearly addressed to OGCM having grid size lying in the mesoscale range, *i.e.* the proposed BBRs parameterisation is suitable for models that reproduce mean flow inhomogeneity even if not fully eddy resolving.

Different diffusivity parameterisations are implemented in a OGCM of the Mediterranean Sea. We compare results from three long-integration experiments using horizontally constant tracer diffusivity, BBRs and Smagorinsky parameterisations. The role of the enstrophy factor in the BBRs parameterisation is highlighted analysing results from a fourth experiment in which diffusivity is proportional only to the eddy kinetic energy. Since our interest is in long-integration experiments for climatic research, we use a model configuration with a relatively coarse resolution ( $0.25^\circ \times 0.25^\circ \times 19$  levels). We study the adjustment of the model to equilibrium and we show that the eddy diffusivity parameterisation is a crucial factor for reproducing and maintaining in long-integration experiments qualitatively correct vertical stratification and basin internal dynamics.

In order to isolate the effect of horizontal varying mixing scheme, we consider in this first work the usual implementation of the MOM code to the Mediterranean, without Redi [11] tensor rotation and without implementation of Gent and Mc Williams [12] bolus velocity parameterisation. In a forthcoming paper we will implement BBRs parameterisation in a more idealized case using isopycnal diffusion.

The layout of this work is as follows. In sect. 2 we outline the theoretical background of the Smagorinsky and BBRs parameterisations; in sect. 3 we resume the main charac-

teristics of the circulation of the Mediterranean Sea; in sect. 4 we analyse the influence of the enstrophy factor in the BBRS parameterisation and in sect. 5 we resume and discuss the results.

## 2. – Eddy diffusivity parameterisations using passive scalars

2.1. *BBRS parameterisation.* – Even if active tracers like temperature and salinity alter the density and the velocity field, in a simple model of diffusivity these tracers can be taken as passive. We consider the particles displacement variance, or structure function,

$$A_L(\tau) = \langle |\underline{x}(t + \tau) - \underline{x}(t)|^2 \rangle,$$

that is related to the total energy frequency Lagrangian spectrum  $P(f)$  by the relation

$$(1) \quad A_L(\tau) = \frac{2}{\pi^2} \int_0^\infty \frac{P(f)}{f^2} \sin^2(\pi\tau f) \, df.$$

It is easy to show that while for small times all frequencies equally contribute to particles displacement, for large times the lower frequencies dominate and eq. (1) can be approximated by [13, 14]

$$A_L(\tau) = 2P(0) \cdot \tau = 4ET_L \cdot \tau \quad \text{for} \quad \tau \gg T_L,$$

where  $T_L = \int_0^\infty R(t) \, dt$  is the Lagrangian correlation time,  $R(t)$  is the Lagrangian velocity correlation function and  $E = \int_0^\infty P(f) \, df$  is the Lagrangian eddy kinetic energy.

For large times ( $\tau \gg T_L$ ), the Lagrangian diffusivity  $K(\tau)$  is then

$$(2) \quad K(\tau) = \frac{1}{2} \frac{d}{d\tau} A_L(\tau) = P(0) = 2ET_L,$$

and it is defined only if the velocity power spectrum saturates at small frequencies. Defining  $e(k)$  as the wave number total energy spectrum, one has that, if  $e(k) \propto k^{-\alpha}$ , the value  $\alpha = 3$  marks the transition from *local* to *non-local* dynamics. In local dynamics ( $\alpha < 3$ ) self-similarity arguments hold and motions on scale  $L$  are dominated by kinetic energy on scale  $L$  [15]. In non-local dynamics ( $\alpha > 3$ ) the motion is dominated by low wave number, the enstrophy ( $Z$ ) converges even in the absence of a high wave number cut-off and the motion is characterised by the time scale  $T$ :

$$(3) \quad T^{-2} = Z = \int_{k_0}^\infty k^2 e(k) \, dk = \int_{k_0}^\infty k^{2-\alpha} \, dk.$$

When the diffusive limit (2) exists, the estimate of  $T_L$  provides a direct way to compute  $K$ , and BBRS showed that in the case of non-local dynamics the Lagrangian correlation time  $T_L$  can be evaluated by means of eq. (3). More precisely, if one assumes that both the Lagrangian and the Eulerian velocity correlation functions are Gaussian in shape, the following relation between  $T_L$  and  $Z$  can be obtained:

$$(4) \quad T_L = C \cdot Z^{-1/2},$$

where

$$C = \left(\frac{2\pi}{3}\right)^{1/2}.$$

Substituting back in eq. (2), the following expression for diffusivity is found:

$$(5) \quad K = \left(\frac{8\pi}{3}\right)^{1/2} \cdot E \cdot Z^{-1/2}.$$

It was shown in BBRS that there is a good agreement between the  $T_L$  computed from (4) and that obtained directly by integrating the Lagrangian particles seeded in different and non-homogeneous subdomains of a 2D turbulent field. Moreover, the estimate of the Lagrangian diffusivity from (5) turned out to be superior to the one obtained assuming  $K$  to be simply proportional to  $E$ . Larcheveque [16] and Hua *et al.* [17] showed the consistency of eq. (5) even if the Gaussian hypothesis seems to overestimate the constant  $C$  in eq. (4).

In this work, expression (5) is used to model the tracer diffusivity. The Eulerian quantities  $E$  and  $Z$  are computed over subdomains in which the flow can be considered homogeneous, *i.e.* in a neighbourhood of the point of size  $L \sim L_E$ , where  $L_E$  is the Eulerian velocity integral length scale computed from model outputs. The resulting diffusivity field is then updated in the model every ten days, *i.e.* with a time lag similar to the Eulerian integral time scale of the velocity field (details on the implementation of the parameterisations are given in Appendix B).

The BBRS parameterisation represents eddy diffusivity processes linked to the meso-scale time and space variability of the dynamics simulated by the OGCM on length scale  $L_E > h$  (where  $h$  is the grid size). It is a *grid scale* processes parameterisation that is suitable for (eddy permitting) models in which turbulence and vorticity are reasonably represented and in which the grid size lies in a range (mesoscale) characterised by steep velocity spectra and non-local dynamics effects.

A peculiar feature of the BBRS parameterisation is the inverse dependence on the square root of enstrophy. It has been observed in many circumstances (*e.g.*, [18]) that in the presence of frontal shears particles, or tracers, can actually be inhibited from dispersing across the velocity front. The decrease of diffusivity in high-vorticity regions stated by (5) is then useful to preserve both the water mass properties and the structure of energetic border currents that are unrealistically broadened in the case of a simple and linear dependence of  $K$  on kinetic energy [8]. Note also that this kind of dependence on the enstrophy makes this parameterisation more suitable for tracers than momentum.

Finally, we want to point out some relation with observed data. Real oceanic spectra seldom exhibits a power-like behaviour over a broad frequency (wave number) range. Experimental spectra from Lagrangian floats [19-22] and from long time series of altimetric TOPEX/POSEIDON data in extra tropical ocean [23] are characterised by a low-frequency (wave number) plateau and by a steep energy decay in the mesoscale range with bilogarithmic spectral slope  $2 < \alpha < 3$ . In regions characterised by strong mesoscale activity  $\alpha > 3$  is often observed, while values closer to 2 are found in less energetic regions. These observational results suggest the importance of low frequencies

and of non-local interactions in oceanic flow <sup>(1)</sup> and have prompted us to test the BBRS parameterisation in a OGCM whose resolution ( $h = 0.25^\circ$ ) can be considered sufficient to partially represent mesoscale activity.

**2.2. Smagorinsky parameterisation.** – Smagorinsky [24] proposed a parameterisation for the eddy viscosity  $\nu$  of the form

$$(6) \quad \nu(x, y, t) = \delta h^2 [N^2(x, y, t) + S^2(x, y, t)]^{1/2},$$

where  $h$  is the grid size,  $\delta$  is a proportionality constant and  $S$  and  $N$  are the velocity shear and normal stress. This parameterisation was devised to model atmosphere dynamics in the 3D isotropic turbulent inertial subrange characterised by a direct energy cascade from low to high space wave number<sup>(2)</sup>. When the model grid size lies in this subrange, *similarity arguments provide insight into the statistical properties of transfer* and it is possible to derive a one-to-one relation between eddy viscosity and horizontal velocity strains that is *locally* valid, *i.e.* eddy viscosity at a given scale depends on the strains at the same scale [26]. Even if Smagorinsky approach was thought to represent subgrid scale momentum transfer processes when the model grid size lies in the inertial range, this parameterisation has also been implemented in numerical oceanographic model (*e.g.*, [27, 28]) using a constant Prandtl number.

It is interesting to emphasize here both the different functional dependence on horizontal velocity gradients and the different conceptual frameworks of the BBRS and Smagorinsky parameterisations. The BBRS parameterisation is valid when dynamics is non-local and it takes into account the variability simulated by the model on scales larger than the grid size. On the other hand, Smagorinsky parameterisation is an extrapolation to the grid size of the unresolved subgrid scale dissipative effects that is valid in the (3D) inertial regime.

### 3. – The Mediterranean Sea circulation

The Mediterranean sea (see fig. 1) is an evaporative basin in which the water deficit is supplied by the surface inflow of Atlantic Water (AW) at Gibraltar. The net result of the air sea interactions in the entire basin is an outflow of denser subsurface water, that is mainly composed by the salty and relatively warm Levantine Intermediate Water (LIW in the following, see, *e.g.*, [29, 30]). LIW is formed in the eastern Levantine basin, sinks to between 200 and 500 meters and, characterised by a salinity relative maximum (SRM, hereafter), spreads out across all the basin at this intermediate depth. Despite this simplified pattern, the circulation in the Mediterranean Sea remains rather complex. Most of the Mediterranean sub-basins are characterised by water mass formation processes and the circulation of deep and intermediate water masses is strongly influenced by mesoscale activity and strong topographic constraints that cause a large spatial variability of the mixing characteristics.

---

<sup>(1)</sup> It can be easily shown that in the presence of a spectrum characterised by a low-frequency plateau followed by a steep energy decay, the low-frequency contribution dominates the dispersion properties for  $\alpha > 2$  [21].

<sup>(2)</sup> Nastrom and Gage [25] observed that while a  $-3$  slope fits the bilogarithmic atmospheric energy spectrum for scales larger than 300–400 km, a  $-5/3$  slope fits well for smaller wavelength ( $2 < \lambda < 300$  km).



Fig. 1. – Mediterranean Basin. Black sea and the Biscay bay are masked in the model. The light gray represents the model buffer zone in the Atlantic and the North Western Mediterranean Sea inside the basin (see text). In the gray area 1 mean profiles of hydrological properties were stored every 5 days during all the experiments.

In the Mediterranean Sea the Rossby radius of deformation varies both seasonally and geographically between  $\sim 5$  and  $\sim 20$  km, but many observations show the existence of eddies on much larger scale (see, for example, [31, 32] and some of these mesoscale features can be developed also with a  $\frac{1}{4}^\circ$  model [33]). In the Eastern Mediterranean deep water is formed in the Adriatic and in the Aegean sea [34, 35], and in the North Western Mediterranean (light gray area in fig. 1 and NWM hereafter) in the Gulf of Lyon [36-38]. The existence of LIW SRM acts as a source of static instability in the winter deep convection—heat forced—in the Gulf of Lyon. Consequently a proper representation of the LIW path is a primary element for a correct numerical simulation of the Mediterranean circulation because deep water formation and LIW dispersal are linked to one another to establish the overall thermohaline circulation [39]. In the Western Mediterranean, experimental observations show either a LIW bifurcation west of Sardinia in two branches [40], respectively going northward to the NWM and westward directly to Gibraltar, or a single northward boundary current west of Sardinia [41, 42]. This area is characterised by strong mesoscale activity with large eddies that, starting from the African Coast, propagate northward both at the surface and in the subsurface layers [32, 43]. Most of the previous numerical studies of the Mediterranean circulation display a predominant westward LIW pathway without the northward branch [44, 45]. In Wu and Haines [39] the northward LIW branch is present only in the first 10 years of the model integration, while in a successive work the same authors [46], using strong temperature surface relaxation constant ( $2h^{-1}$ ) and very low diffusivity and viscosity eddy coefficients, maintained for a 120 years simulation the northward LIW transport with the related realistic vertical stratification. As pointed out by the authors, the unsatisfactory aspects of their simulation are the strong constraints in the surface circulation and the occurrence of numerical instabilities, due to the low diffusivity and viscosity eddy coefficients. Even with these minor lacks, this simulation is successful in reproducing the Mediterranean thermohaline circulation on time scales comparable with the basin renewal time. The aim of this work is to reach the same result by working on the internal

TABLE I. – *Tracer eddy diffusivity parameterisations for the different experiments. The vertical profile of EXP1 experiment is obtained by averaging in the horizontal the values of the diffusivity field stored every 10 days in the 150th year of integration of EXP2.*

Experiment	Tracer eddy diffusivity parameterisations
EXP1	Vertical profile from EXP2 constant in the horizontal plane
EXP2	BBRS parameterisation
EXP3	Smagorinsky parameterisation
EXP4	$K \propto E$

model dynamics, introducing an eddy diffusivity parameterisation capable to represent the complicated water masses mixing processes of the Mediterranean circulation.

#### 4. – Results

4.1. *Numerical experiments.* – Four different eddy diffusivity parameterisations (table I) are implemented in a Bryan-Cox numerical model applied to the Mediterranean Sea [39,44,47-49]; details on the model configuration and on the estimation of the diapycnal mixing implicit in the horizontal mixing scheme are given in Appendix A).

In EXP2 and EXP3 the BBRS and Smagorinsky parameterisations are used, respectively. To highlight the role of the horizontal variability of  $K$ , EXP1 is performed assuming for the horizontal diffusivity the vertical profile obtained horizontally averaging the mean diffusivity field of EXP2. Finally, to analyse the influence of the enstrophy factor in the BBRS parameterisation we carried out a fourth experiment in which the eddy coefficient is proportional to the eddy kinetic energy  $E$  (EXP4,  $K = c \cdot E$ , where  $E$  is computed in the same way as in EXP2). We do not discuss here results from a further

TABLE II. – *Time variability of the spatial mean of the diffusivity coefficient. Values are expressed in  $10^5 \text{ cm}^2/\text{s}$ . Spatial mean (for EXP2, EXP3 and EXP4) are relative to the whole basin and are computed using ten days snapshots of the 150th year of integration.*

	Max.	Min.	Mean
EXP1	6.0	6.0	6.0
EXP2	7.0 April	5.5 November	6.0
EXP3	5.3 March	4.6 November	4.9
EXP4	8.3 April	6.0 November	7.2

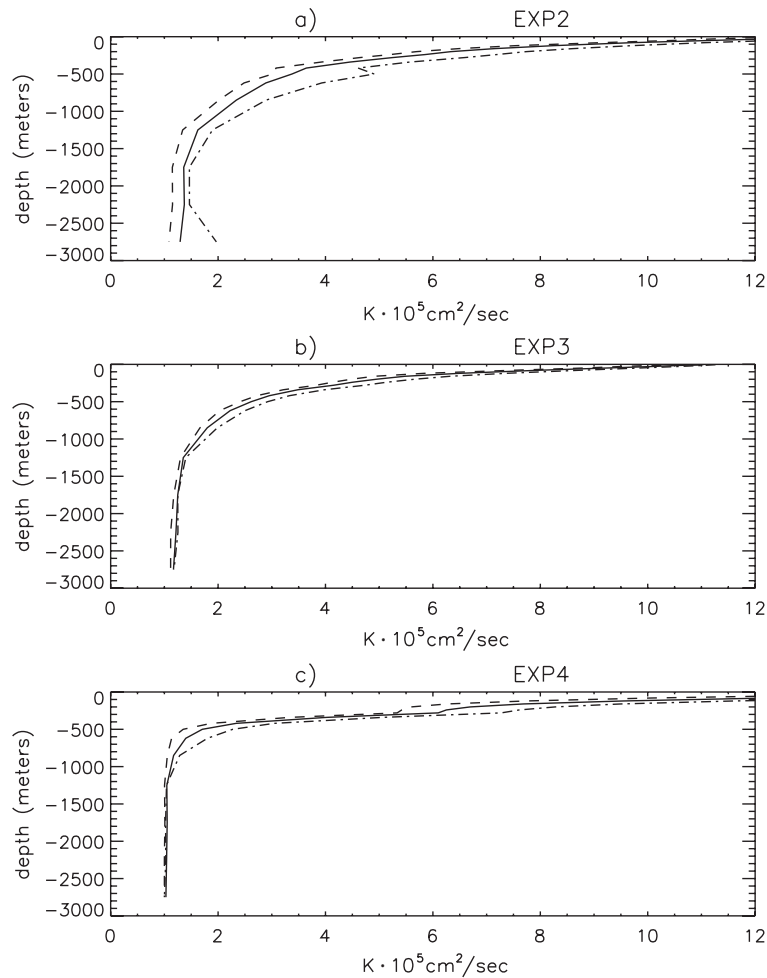


Fig. 2. – Winter, autumn and yearly mean (dashed and dotted, dashed and full line, respectively) vertical profiles of diffusivity for EXP2, EXP3 and EXP4 (panels a, b and c). The yearly means were obtained from diffusivity field stored every 10 days in the 150th year of integration.

experiment (EXP0) with constant  $K$  both in the vertical and the horizontal direction since they are qualitatively similar to those of EXP1.

The horizontal diffusion of a tracer  $Q$  is represented as a second-order operator *diffusion* =  $\nabla_h \cdot (K \nabla_h Q)$ , where  $\nabla_h$  is the horizontal gradient. All the experiments, that differ only in the parameterisation of the tracers horizontal diffusivity coefficient  $K$ , are integrated up to 300 years and different parameters, like the mean temperature and salinity profiles in pre-selected areas, were stored during the runs every 5 days (see fig. 1).

**4.2. Variability of diffusivity field.** – The 3D mean values of the diffusivity coefficient computed in the whole basin (table II) are similar in the four experiments, while its time variability in EXP2, EXP3 and EXP4 shows a maximum in April (EXP2 and EXP4) and March (EXP3) and a fall minimum in November. In these experiments diffusivity decreases with  $z$  down to  $\sim 1000$  m, to assume in the deepest layers  $K$  an approximately constant value (fig. 2).



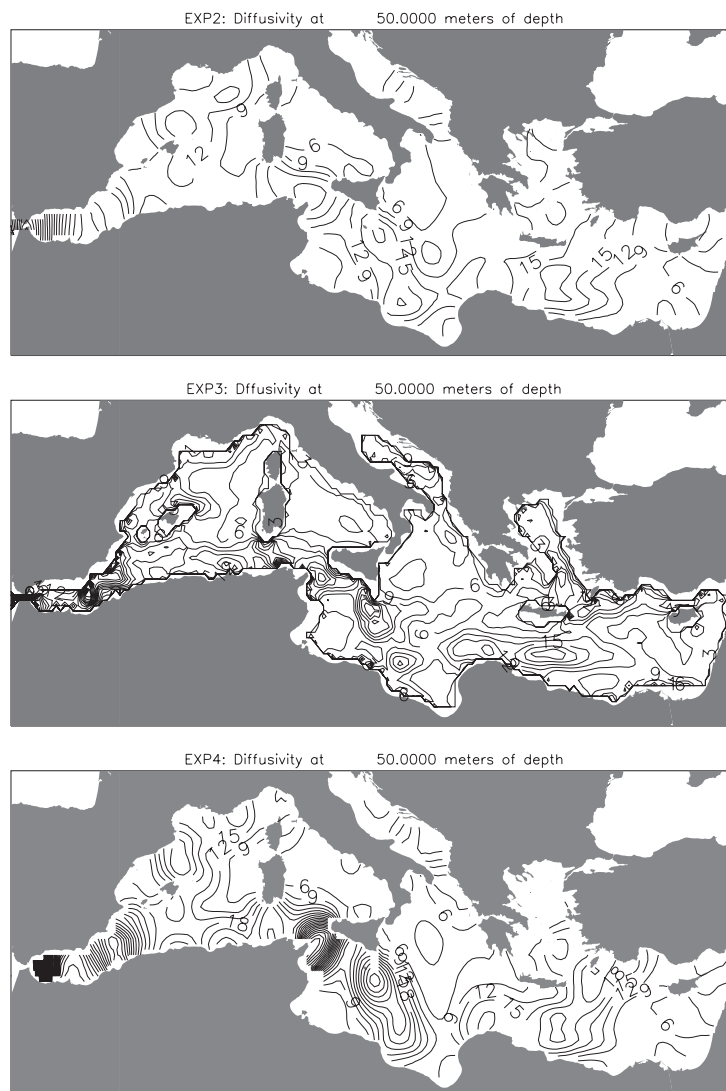


Fig. 3a. – Yearly mean diffusivity field at 50 meters of depth for EXP2, EXP3 and EXP4. The mean values were obtained as described in the caption of fig. 2 and are expressed in  $10^5 \text{ cm}^2/\text{s}$ . Isolines are drawn every  $3 \cdot 10^5 \text{ cm}^2/\text{s}$ .

In the upper layers the diffusivity drops less sharply in EXP2 that moreover displays a slightly larger seasonal variability, with a winter relative maximum of  $K$  in the LIW layers. Figures 3, showing the horizontal maps of the mean diffusivity field computed at 50 (3a) and 340 (3b) meters of depth, give an idea of the huge variability of  $K$ , that can differ at the same depth by two orders of magnitude. The diffusivity fields of EXP2 and EXP4 are smoother and characterised by larger-scale structures (up to sub-basin scale). On the contrary, in Smagorinsky's case (EXP3) isolated maxima are localized in regions of strong velocity shears, such as the Algerian Current. In the Sicily and Gibraltar

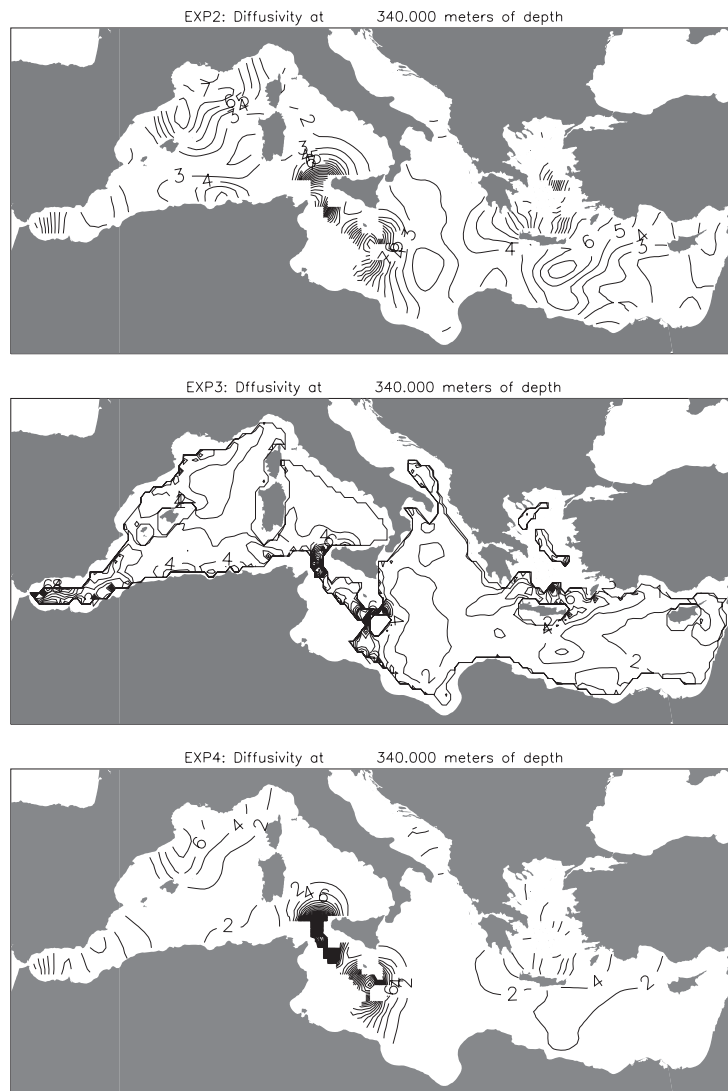


Fig. 3b. – Yearly mean diffusivity field at 340 meters of depth for EXP2, EXP3 and EXP4. The mean values were obtained as described in the caption of fig. 2 and are expressed in  $10^5 \text{ cm}^2/\text{s}$ . For graphical purposes isolines are drawn every  $10^5 \text{ cm}^2/\text{s}$  for EXP2 and  $2 \cdot 10^5 \text{ cm}^2/\text{s}$  for EXP3 and EXP4.

Straits the three experiments are characterised by local maxima of diffusivity that well represent the strong influence of the bathymetry on diffusivity processes. Finally note that in EXP2 the diffusivity field displays well-defined structures in the Lyon Gulf and Rhodes gyre regions, where diffusivity isolines reproduce the gyres structure (see sect. 5).

4.3. *Temperature drift.* – To show the evolution of the model toward equilibrium, we plot in fig. 4a) for the four experiments the yearly basin averaged temperature *vs.* time. The temperature drift observed in EXP1 (dotted line) is definitely reduced in the

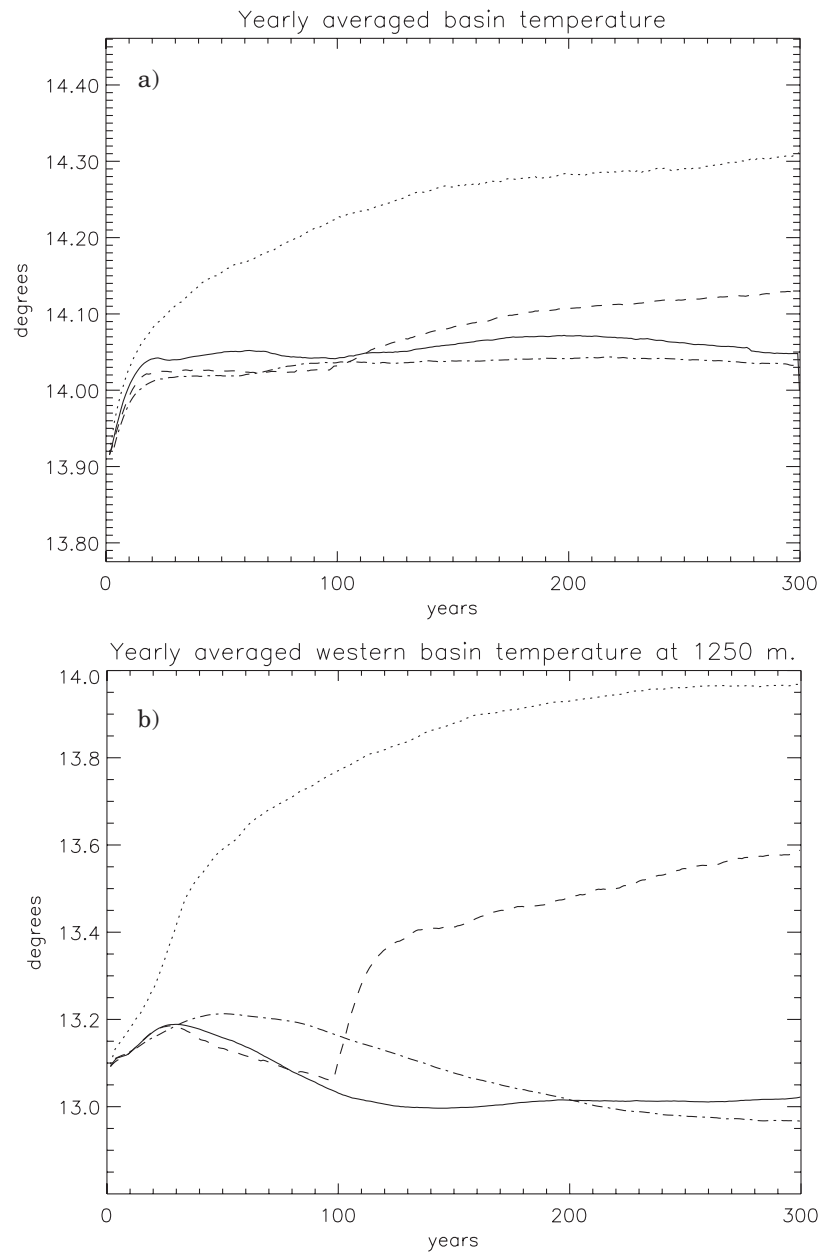


Fig. 4. – Panel a) yearly averaged all basin temperature for EXP1, EXP2, EXP3 and EXP4 (dotted, full, dashed and dash-dotted line, respectively). Panel b) yearly averaged basin temperature at 1250 m of depth in the Western basin for EXP1, EXP2, EXP3 and EXP4 (dotted, full, dashed and dash-dotted line, respectively). The time series are obtained averaging over one year the space mean temperature computed and stored every 5 days during the experiments and do not show the seasonal cycle. The temperature value at  $t = 0$  is the basin averaged climatological MODB MED5 mean temperature.

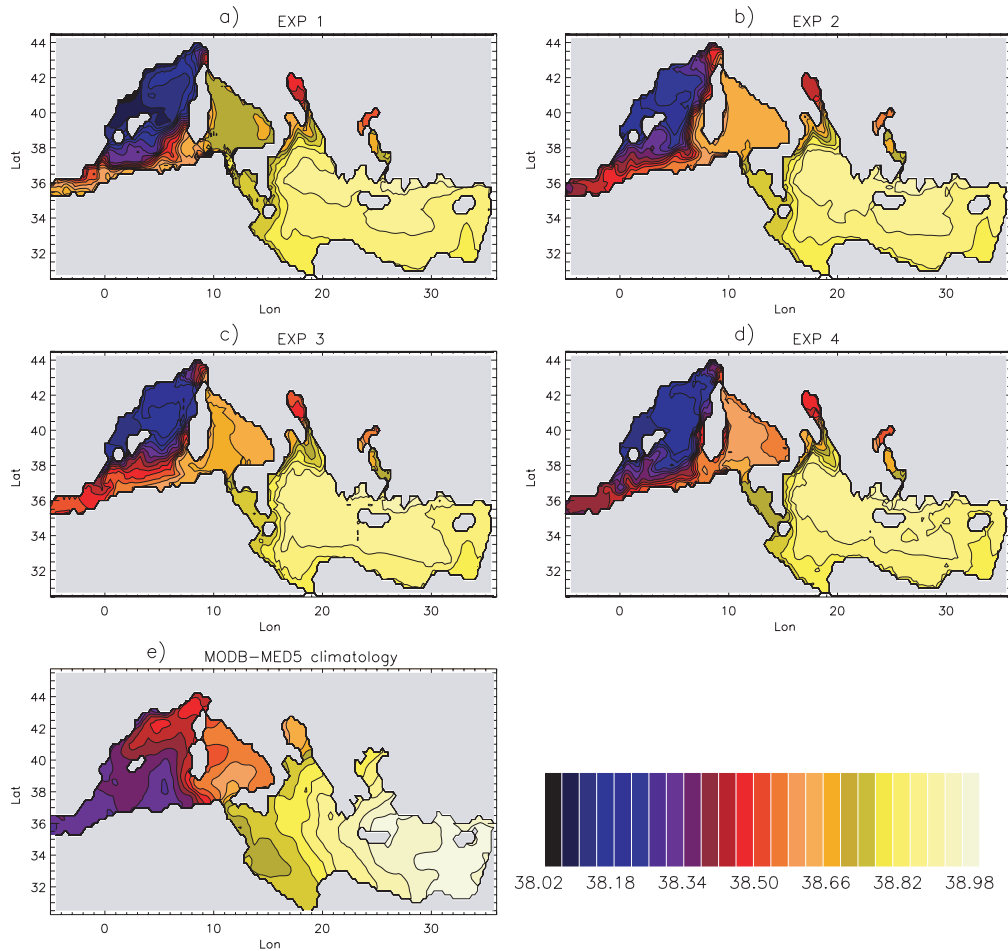


Fig. 5. – Salinity at 340 m of depth from ten-years (150th-160th) averaged field of EXP1, EXP2, EXP3 and EXP4 (panels a, b, c, and d, respectively) and from MODB-MED5 climatology (panel e).

experiments with horizontally varying diffusivity. In particular in EXP2 (full line) the mean basin temperature reaches, after a transient of approximately 20 years, a stable value ( $\bar{T} \sim 14.05 \pm 0.01^\circ\text{C}$ ) that is maintained during the entire run. The warming observed in EXP1 is probably due to a lack of convection in the NWM (see figs. 8 and 9). In fact in EXP3 the deep layer temperature (dashed line in fig. 4b) starts to increase when convection becomes shallower (see discussion of the next subsection and fig. 8), after approximately 100 years of integration.

**4.4. Tracer and velocity fields.** – In fig. 5 are shown the 10-years averaged four (150th-160th) salinity fields from the experiments and the climatological field from MODB-MED5 at 340 meters of depth, which in most parts of the basin corresponds to the depth of the LIW core. In EXP1 (fig. 5a) the LIW crosses the Sicily strait and spreads in the Tyrrhenian basin with almost unchanged—and unrealistic—salinity values, while all the

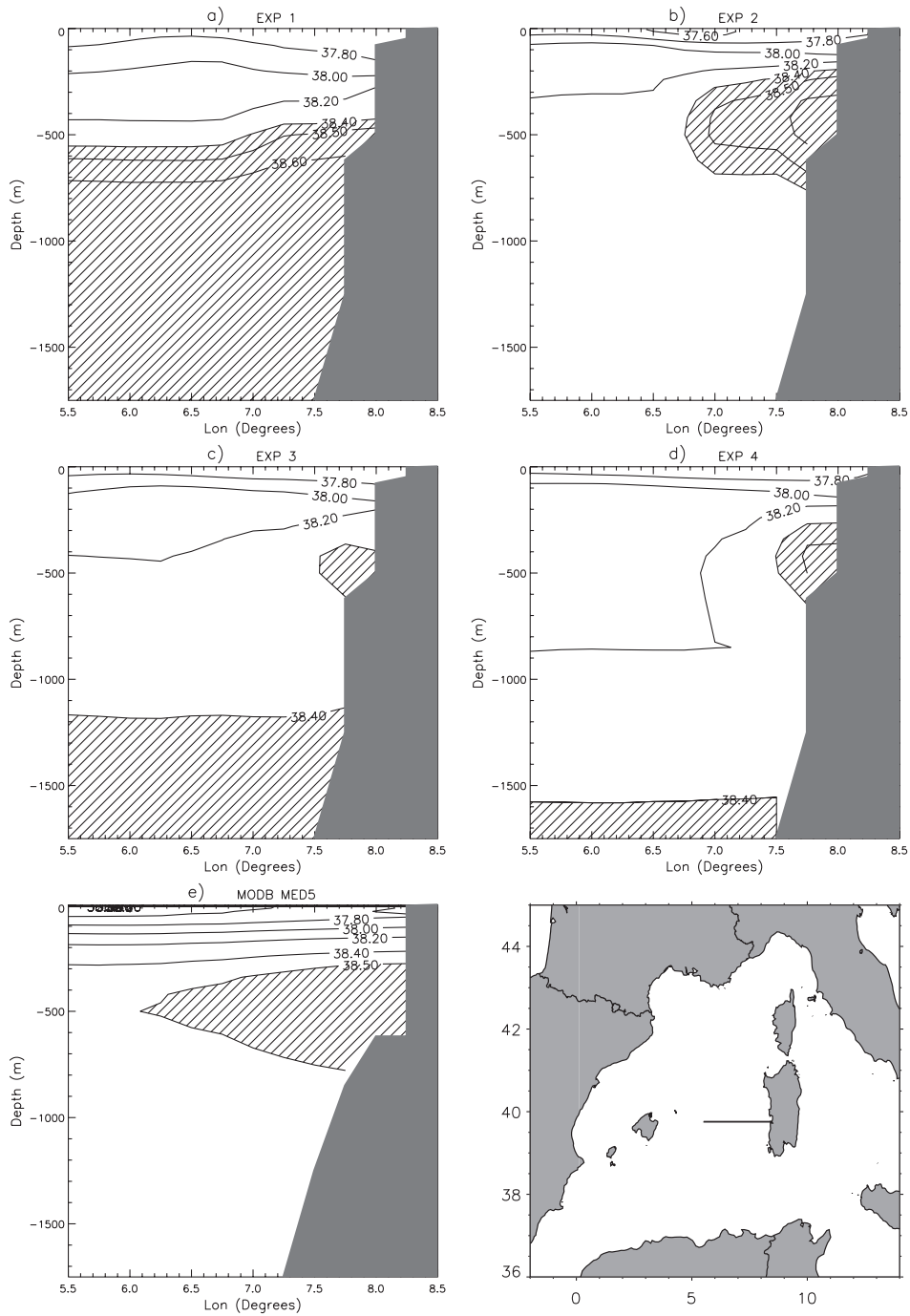


Fig. 6. – Ten-years averaged (150th-160th) salinity section at 40° N for EXP1,EXP2, EXP3, EXP4 and MODB MED5 climatology EXP4. Isolines are drawn every 0.02 up to 38.4 PSU and then every 0.01 PSU. The dashed area represents salinity greater than 38.4 for EXP1, EXP2 EXP3 and EXP4 and greater than 38.5 for MODB MED5 climatology.



Fig. 7. – Position of particles initially released in a section joining Sardinia to Africa (black line) at different time delay (200, 300, 400, 800 and 2800 days for rows top to bottom) for EXP1, EXP2, EXP3 and EXP4 (column a, b, c and d, respectively). Lines joining particles 10 days apart are drawn, giving an indication of particle speed. Particles position are obtained integrating off line the 150th year mean velocity field with the algorithm proposed by Blanke and Raynaud [52].

space- and time-dependent diffusivity parameterisations definitely improve the mixing in the Sicily strait. Salinity in the Tyrrhenian basin changes from values exceeding  $\sim 38.7$  to  $\sim 38.5$ – $38.6$  PSU, in better agreement with experimental data [50]. Results from EXP2 and EXP4 exhibit a more efficient northward spreading of the LIW west of Sardinia, in agreement with observational results [40, 42, 43, 51], which leads to an important salt

excess of  $\sim 0.1$ – $0.2$  PSU in the area of the Gulf of Lyon. On the contrary, in EXP1 and EXP3 the salinity distribution displays a predominantly westward propagation of the LIW along north Africa’s coasts with higher and lower values in the Alboean Sea and in the NWM, respectively. In EXP2 and EXP4 this westward LIW branch is thinner, and it is more localized near the African Coast.

From fig. 6, where we plot a vertical section of the 10-years averaged (150th–160th) salinity field west of Sardinia at  $40^\circ$  N for all the experiments and for the MED5 MODB climatology [42], it is evident that only EXP2 qualitatively reproduces the correct vertical stratification with a well-defined subsurface SRM overlying fresher water. In EXP1 the vertical stratification is completely wasted with no sign of subsurface SRM, while in EXP3 and EXP4 the LIW vein is smaller and the salinity increases in the deeper layers. Moreover, EXP2 better represents the northwestern meridional overturning cell with the northward stream of salty LIW, overlying a deeper southward fresher layer (not shown here), that maintains the SRM in the NWM (see fig. 10). The differences in the LIW path in the various experiments are even more evident in fig. 7, where the positions are displayed of about 1000 particles released in a section joining Sardinia to Africa at the averaged depth of 400 m: in EXP1 and EXP3 most of particles go straight to Gibraltar, while in EXP4, and especially in EXP2, a bifurcation is observed and many particles enter in the NWM where move cyclonically and sink to greater depths before reaching the Alboean Sea, flowing westward with a weaker and deeper westward current along the African coast.

In fig. 8 we report (panels a, b, c and d) for the four experiments the time series of the deep convection depth that is defined as the maximum depth  $z$  in which  $\rho(z) < \rho(0) + 0.01$ , where  $z = 0$  is the sea surface and  $\rho(z)$  is the density obtained from the mean profiles of temperature and salinity of region 1 of fig. 1. Note that this definition underestimates the maximum convection depth since the vertical profiles are averaged in a box ( $4 \times 8$  grid points) that is larger than the area where the simulated convection occurs. EXP2 is characterised by the deepest convection, that after  $\sim 100$  years of integration reaches, and stably maintains, the mean depth of 850 m. Deep convection events occur in March with some inter-annual variability that is not analysed here. The time behavior of the development of the mixed layer and the duration of the “numerical” convection events ( $\sim 10$  days, see panel e of fig. 8) result to be in good agreement with available experimental data (*e.g.*, [38]). In fig. 9 we show for the four experiments the homogenization depth reached during a convection event in the 150th year of integration. EXP1 definitely gives the worst result, while the largest convection depth ( $> 1000$  m) is reached by EXP2. The homogenized water column in EXP2 is shallower and less dense ( $\sim 28.94$ ) than in the real case (real deep convection can vary from 500 to 2000 meters of depth with a density value of  $\sim 29.08$ – $29.10$ ; see, for example, [38]). Artale *et al.* [49] using daily surface fluxes in a similar model reproduced the penetration of the mixed layer till the depth of 2000 m. In the context of this work, it is interesting to outline that improvements in the model’s capability to represent deep convection can be obtained only by changing the horizontal diffusivity parameterisation.

To better understand and describe the scenario, we plot in fig. 10 the salinity, temperature and density vertical profiles of region 1 (see fig. 1) before, during and after the convection event of the 200th year of integration. In EXP2 (panels d, e, f) the real salinity vertical structure is reproduced with the LIW SRM that is eroded and reconstructed during and after the convection event. Neither in EXP3 (panels g, h and i) nor in EXP1 (panels a, b and c) the correct vertical structure is reproduced, while in EXP4 the SRM is less pronounced and salinity grows in the deepest layers. Finally, note that the tem-

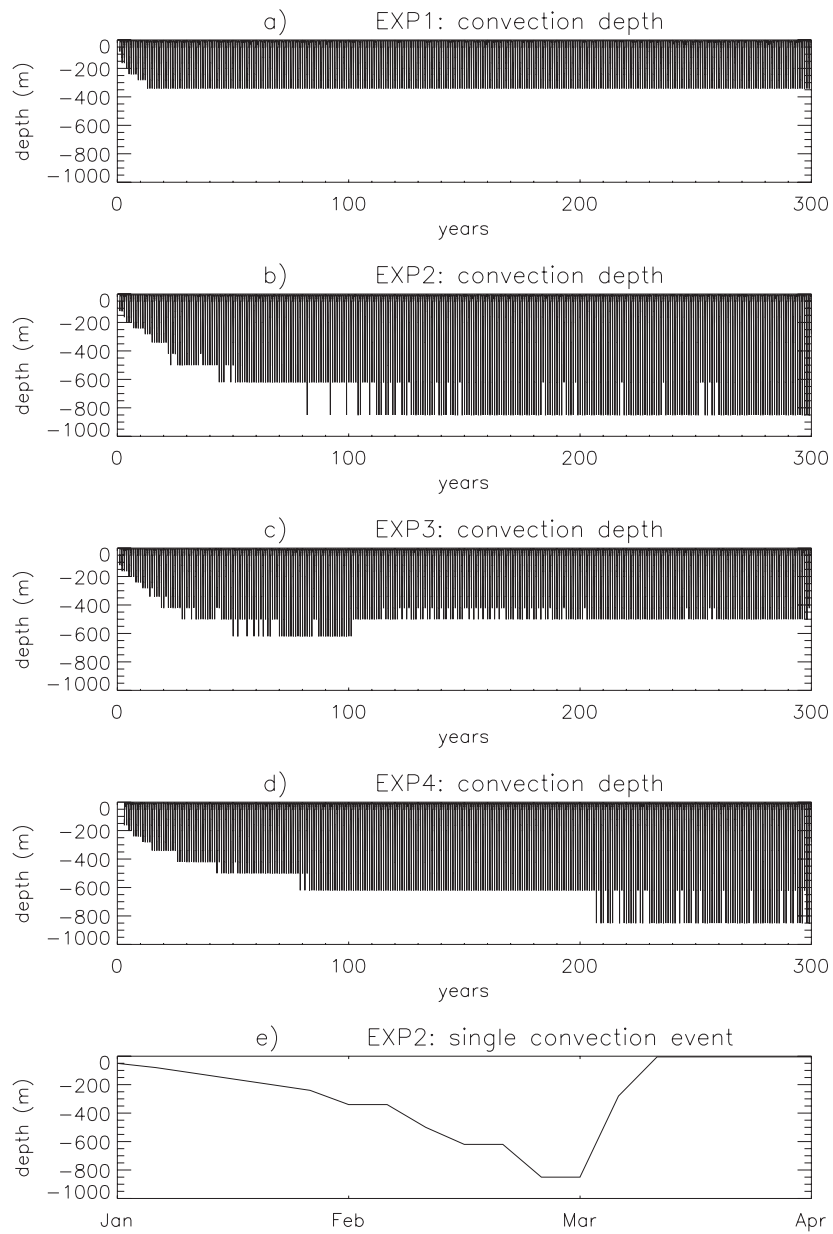


Fig. 8. – Convection depth (see definition in the text) in the Gulf of Lyon as a function of time for EXP1, EXP2, EXP3 and EXP4 (panels a, b, c and d). Panel e: time behavior of a single convection event in EXP2.



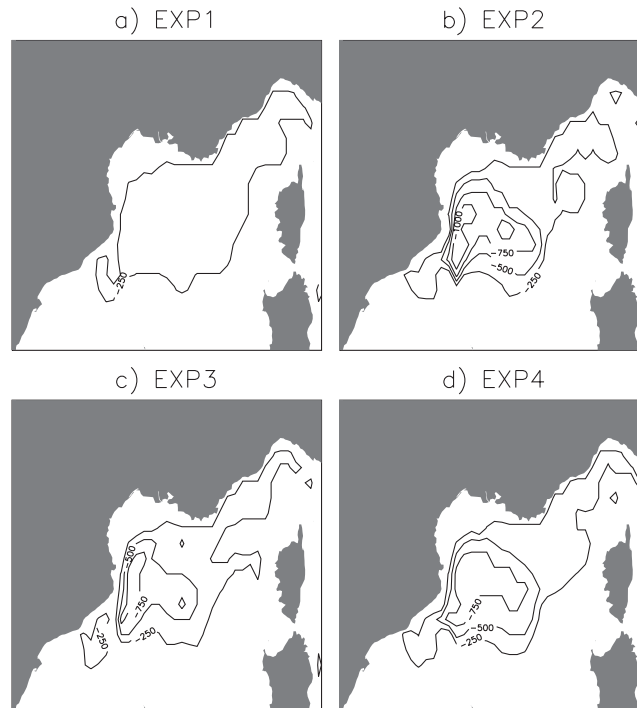


Fig. 9. – Isolines of convection depth during the deep convection event of the 160th year of integration for EXP1, EXP2, EXP3 and EXP4.

perature of the deep layers is inversely proportional to the convection depth reached in the different experiments.

All the results shown here indicate that EXP2 definitely displays the best performance, with a well-defined meridional overturning cell in the NWM, the deepest convection and a realistic and qualitatively correct vertical distribution of the hydrological properties. The subsurface salty layer in the NWM is a source of instability in the winter convection and it is maintained by the northward LIW branch that is in turn strengthened by the more efficient deep convection. It is not easy to understand which is the driving mechanism, *i.e.* if it is the deep convection that drives the overturning cell or, vice versa, if it is the most efficient northward salt transport the primary cause for the better deep convection simulation. The two phenomena are intimately linked; in the next section we will try to clarify the feedback effects investigating the effect of the BBRS parameterisation in the representation of gyres.

**4.5. Dynamical equilibrium of the model.** – We already noted that in EXP2, EXP3 and EXP4 the mean basin hydrological values reach stable values after approximately 20 years of integration (subsect. 4.3, fig. 4a). Here we discuss the different time scales observed in the settlement to the equilibrium between water masses dynamics and surface forcing (perpetual year with monthly fields, see Appendix A for details). In fig. 11 we plot the mean LIW layers salinity in the NWM as a function of time, for EXP2 (full line) and EXP3 (dashed line). In EXP2 the initial conditions are rapidly modified and the salinity initially decreases with an e-folding time of  $\sim 20$ –30 years. This freshening

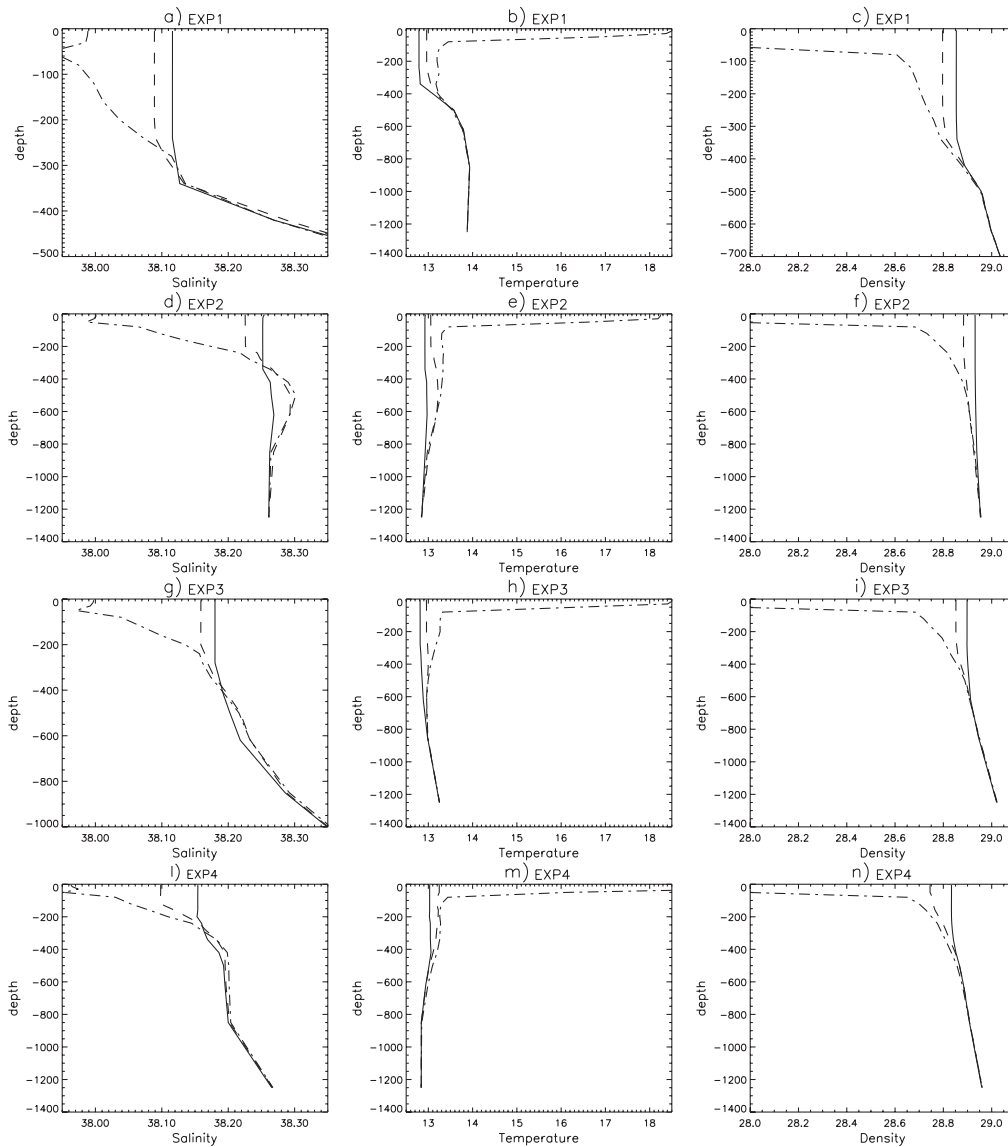


Fig. 10. – Salinity, temperature and density profiles averaged in region 1 of fig. 1 in the first 1200 meters before (winter, dashed line), during (full line) and after (summer, dashed and dotted line) the convection event of the 200th year of integration for EXP1 (panels a, b and c), EXP2 (panels d, e and f), EXP3 (panels g, h and i) and EXP4 (panels l, m and n).

of LIW layers ends after approximately 60 years and salinity starts to slowly increase after  $\sim 100$  years of integration to reach after  $\sim 150$  years a constant value  $\sim 38.26$  PSU, representative of a new equilibrium.

In EXP3 the “loss of memory of the initial conditions” is slower; in the first 100 years salinity is greater than in EXP2, but at the 102th year of integration a sudden decrease of both LIW layer salinity and convection depth (fig. 8, panel c) is observed. To describe

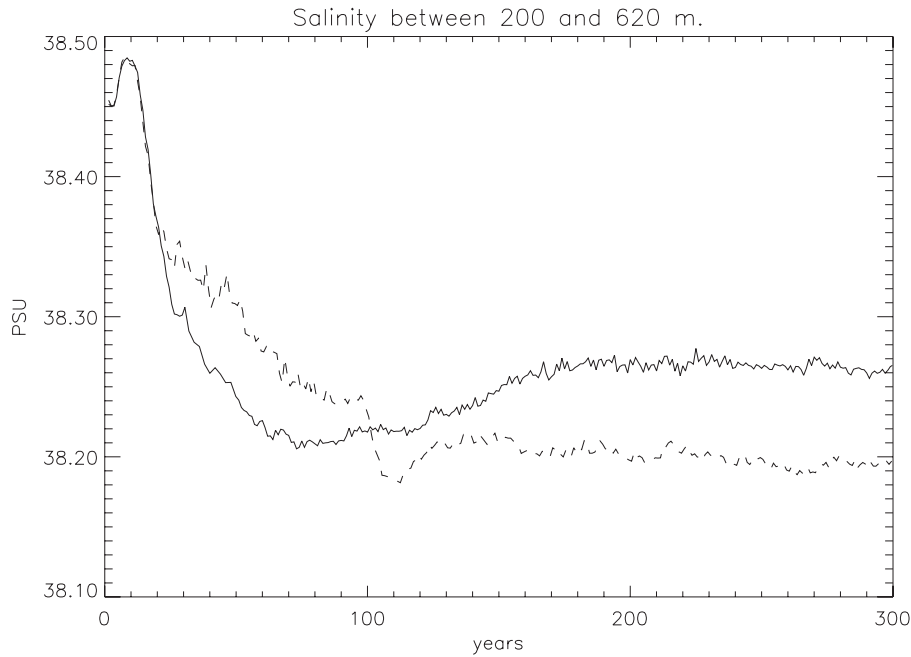


Fig. 11. – Averaged salinity between 200 and 620 meters *vs.* time in the NWM (light gray area of fig. 1) for EXP2 (full line) and EXP3 (dashed line).

the evolution toward the dynamical equilibrium, we plot in fig. 12 the time behaviour of the value and the depth of the SRM in the NWM. In the first years ( $t \sim 30\text{--}40$  years) EXP2 shows a rapid breaking off of the vertical stratification with a sinking of SRM to an unrealistic depth (panels c and d of fig. 12). The vertical stratification with a SRM at a realistic depth is reconstructed only after  $\sim 50$  years when the convection depth begins to be greater or equal to the SRM depth (see panel b of fig. 8) and the model starts to produce deep water (deeper than LIW). After  $\sim 100$  years a deepening of convection is observed together with a stabilization to a shallow depth of SRM that simultaneously begins to slowly grow to reach a stable value of  $\sim 38.32$  after 150 years of integration. The convection deepening observed after  $\sim 100$  years is linked both to the SRM growth and to its stabilization to shallower depth. Likewise, note how a stable equilibrium between the surface forcing and the internal water masses dynamics is reached (and maintained for the rest of the experiment) only after  $\sim 100$  years of integration. At this time the initial condition's waters have been replaced by new model waters and the reached equilibrium qualitatively represents the circulation of the NWM, with correct vertical stratification, deep water formation and well-defined meridional overturning cell in the northwestern part of the basin. This is not the case in either EXP1 or EXP3. In EXP1 the SRM progressively grows and sinks to an unrealistic depth, greater than the observed convection. EXP3 shows, in the first years of integration, a behaviour similar to that of EXP2, with a smaller deepening of SRM ( $0 \sim 30$  years) followed by a stabilization of SRM depth at  $\sim 600$  m. In contrast to the EXP2 case the SRM does not raise to shallow depth for larger times. The convection depth remains approximately equal to the SRM depth until year 102, when the vertical structure of the salinity is broken and

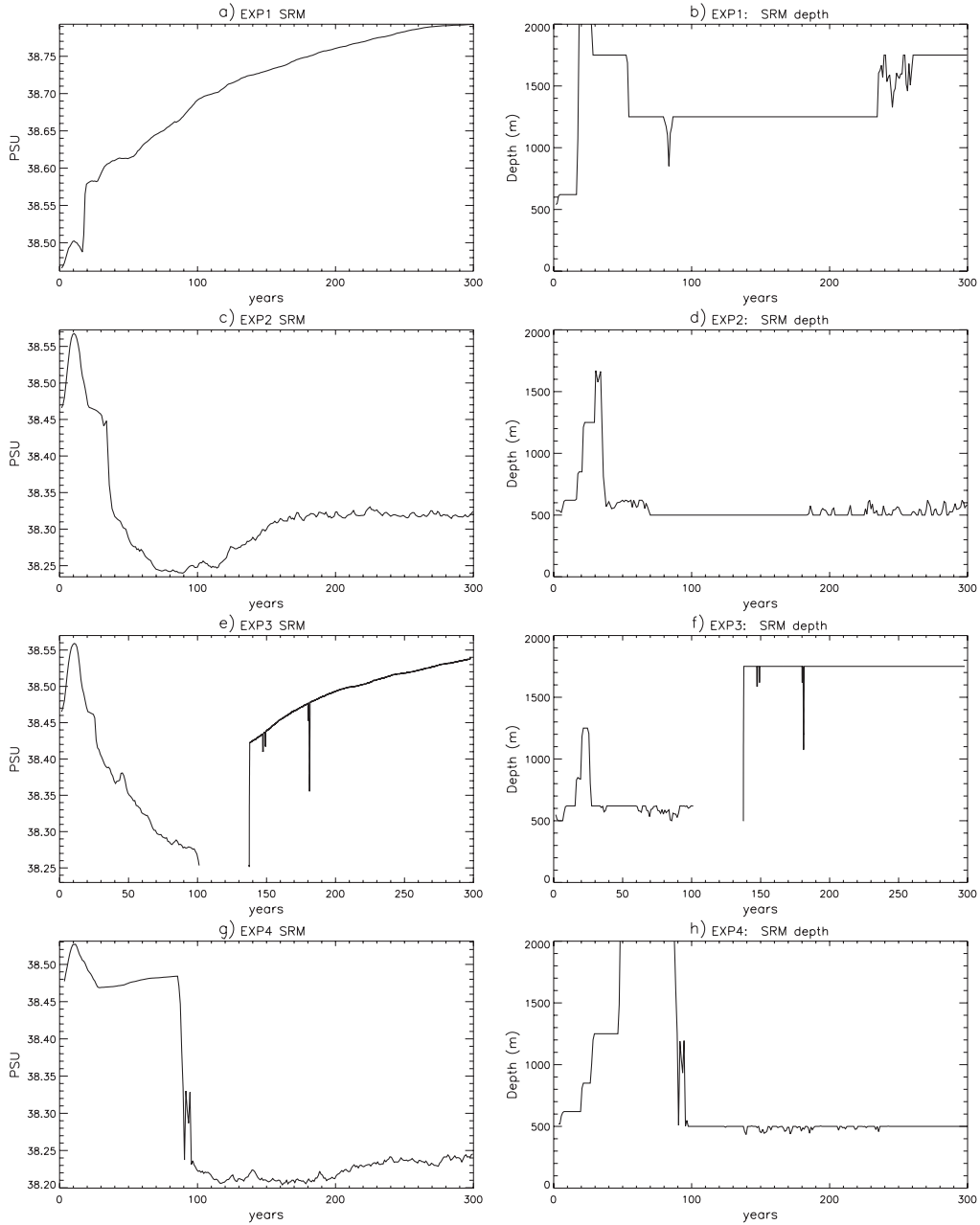


Fig. 12. – Salinity relative maximum and its depth *vs.* time in NWM for EXP1 (panels a and b), EXP2 (panels c and d), EXP3 (panels e and f) and EXP4 (panels g and h). Between  $\sim 115$  and  $\sim 138$  years there is no SRM in EXP3.

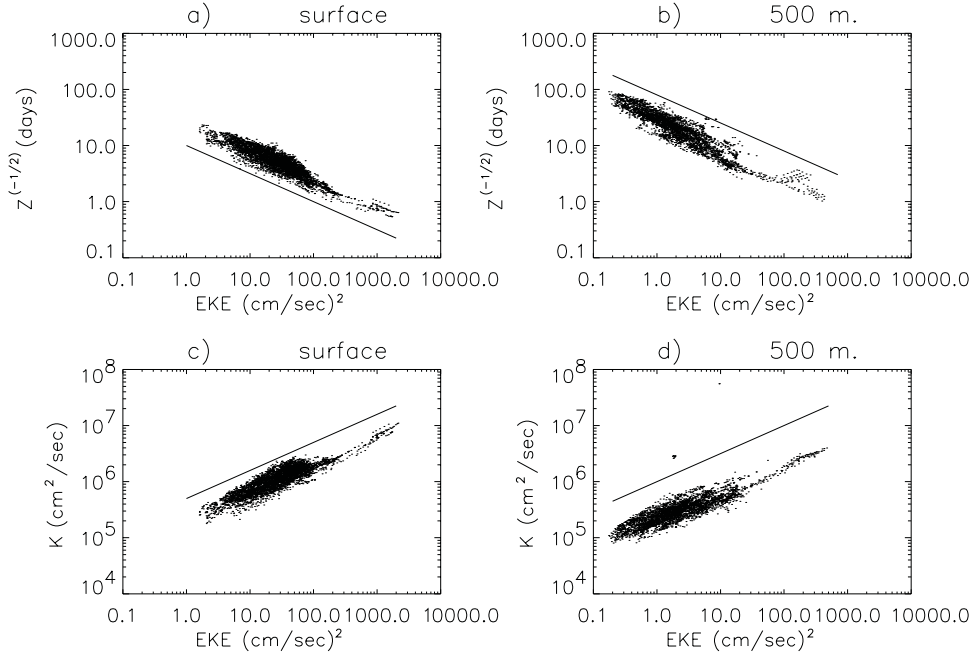


Fig. 13. – Bilogarithmic scatter plot of ten-years averaged values of  $Z^{-1/2}$  and  $K$  (estimated by (5)) vs. eddy kinetic energy in the Mediterranean computational domain at the surface (panels a and c) and at 500 m of depth (panels b and d). Power law  $E^{1/2}$  and  $E^{-1/2}$  are superposed. The ten years means were obtained averaging daily values from the 150th to the 160th model year integration.

the system collapses. The SRM first sinks to the bottom, then disappears and finally settles down at an unrealistic depth ( $\sim 1700$  m for  $t > 150$  years), much greater than the convection depth ( $\sim 600$  m): there is no deep water formation (deeper than LIW) and the vertical structure of the salinity is unrealistic. The breaking off of the salinity vertical structure in EXP3 (namely the disappearance of the SRM in the subsurface layer) precedes the first event in which convection becomes shallower (approximately after 102 years, see panel c of fig. 8): deep convection occurs only when the subsurface SRM exists and is at a right depth but, on the other hand, the SRM disappears after some years of *intermediate* convection.

EXP4 displays a behaviour qualitatively similar to EXP2 but with different time scales: convection depth becomes definitively deeper than SRM only after  $\sim 200$  year of integration.

## 5. – The role of the enstrophy factor in BBRS parameterisation

To evaluate the impact of the enstrophy factor in the BBRS parameterisation we show in fig. 13 the scatter plot of the ten years averaged (150th-160th) values of  $Z^{-1/2}$  and  $K$  (estimated from eq. (5)) vs. the eddy kinetic energy, both at the surface and at 500 meters of depth. The values of  $Z^{-1/2}$  (that following (4) is proportional to  $T_L$ ) increase with depth and scale approximately as  $\sim E^{-1/2}$ . This power law behaviour is more evident for high energy values while for intermediate energy values the scattering increases.

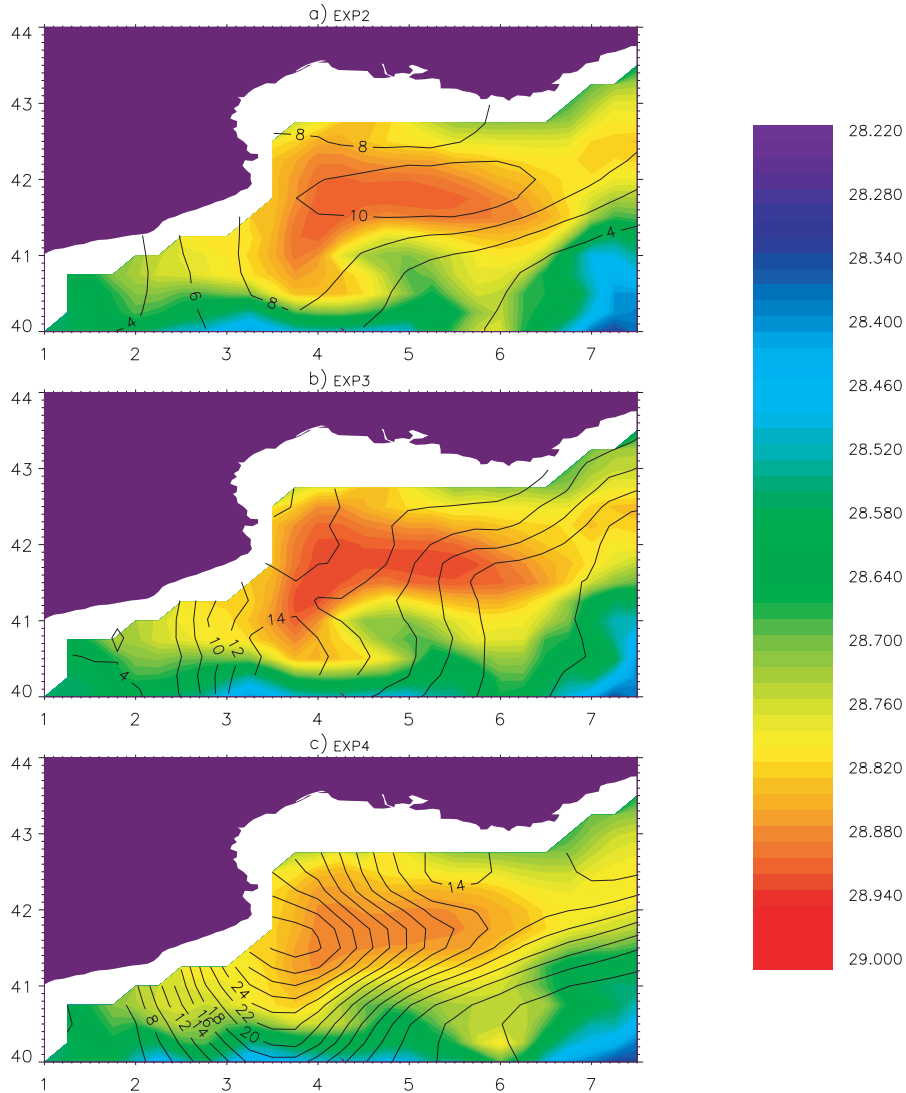


Fig. 14. – February monthly mean (convection preconditioning phase) of density with superimposed diffusivity values at 80 meters of depth for EXP2, EXP3 and EXP4 in the area of the Gulf of Lyon (panels a, b and c, respectively). Colours represent density, isolines of diffusivity are expressed in  $10^5 \text{ cm}^2/\text{s}$ . Monthly mean values of diffusivity and density are relative to the 150th year of integration.

It is difficult to derive from experimental data exhaustive statistical relations between  $E$  and  $T_L$ , but Krauss and Bönning [20] found, from analysis of North Atlantic floats, the same scaling relation  $T_L \sim E^{-1/2}$ . Note that this dependence implicitly states that diffusivity scales approximately as  $K \sim E^{1/2}$  (fig. 13) and that eddies have dimension  $L_{\text{ed}} \sim E^{1/2} \cdot T_L = \text{const}$  independent of  $E$  [53].

The introduction of  $T_L \propto Z^{-1/2}$  in the diffusivity expression then contributes to increase its value with depth (see in fig. 2 the different vertical profile of  $K$  observed in

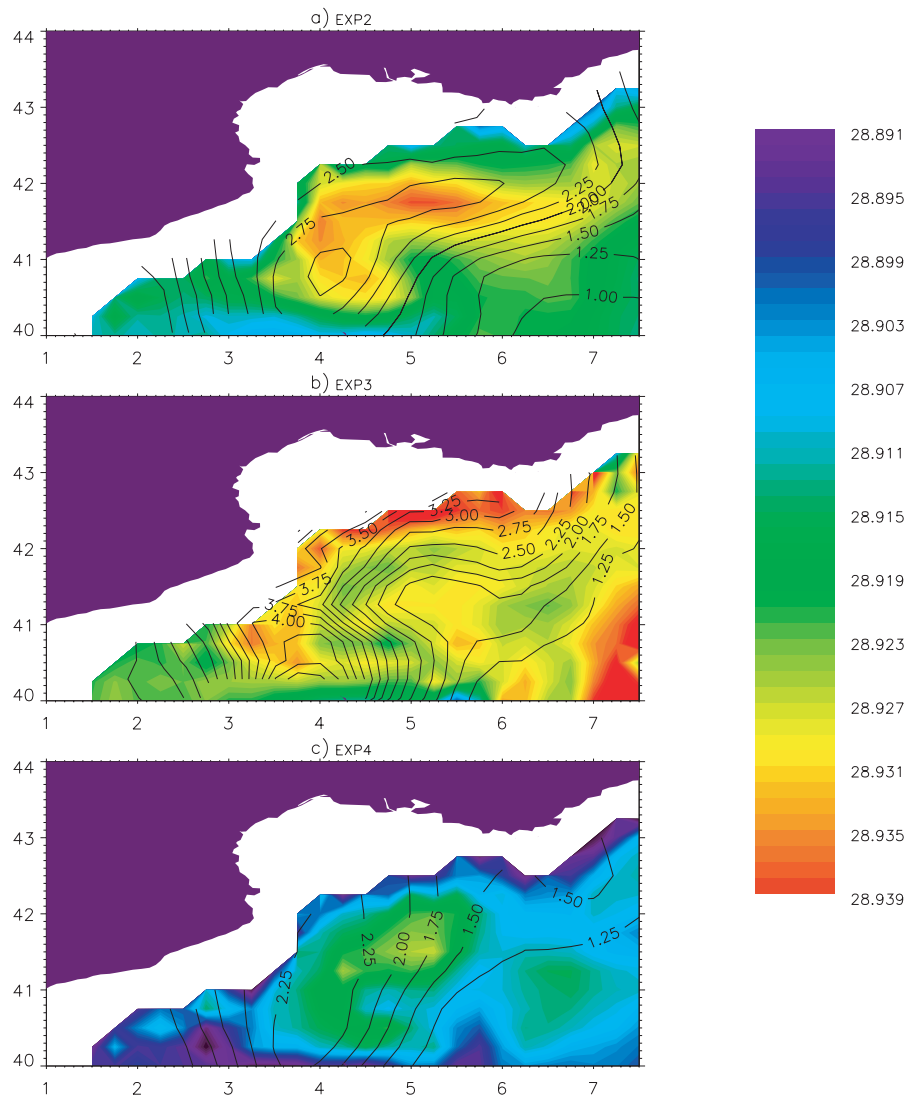


Fig. 15. – February monthly mean (convection preconditioning phase) of density with superimposed diffusivity values at 850 meters of depth for EXP2, EXP3 and EXP4 in the area of the Gulf of Lyon (panels a, b and c, respectively) Colours represent density, isolines of diffusivity are expressed in  $10^5 \text{ cm}^2/\text{s}$ . Monthly mean values of diffusivity and density are relative to the 150th year of integration.

EXP2 and EXP4) and to decrease it in strongly energetic and in high vorticity regions. For instance, the combination of the spatial structures of  $E$  and  $Z$  in the area of the Gulf of Lyon (figs. 14 and 15, but see also fig. 3b for the Rhodes Gyre) leads to a well-defined gyre structure in the diffusivity field with maximal values in the interior of the structure, where the vorticity has a minimum. This maximum of the diffusivity homogenizes tracers in the interior of the gyre, stabilizing it in the convection preconditioning phase. Moreover, the minimal values reached on the strong vorticity border regions inhibit the

cross frontal mixing and mimic the dynamical barrier given by the edge of the gyre. These characteristics are useful to simulate in a coarse resolution model the persistence of coherent structures with the relative trapping of tracers inside it. In the case of the Gulf of Lyon gyre, BBRS parameterisation leads to a stronger and better defined cyclonic structure that persists also in the deeper layers (fig. 15, panel a). On the contrary, in EXP3 and EXP4 diffusivity reaches the maximal values on the edge of the gyre (fig. 14, panels b and c) and far from the surface forcing the cyclonic structure is almost entirely loosen (fig. 15, panels b and c).

## 6. – Summary of the results

We studied, using different mixing schemes, the influence of the variability of the horizontal diffusivity on the circulation of the Mediterranean, and we proposed for the first time the application of the BBRS eddy diffusivity parameterisation to a OGCM.

It was found that the horizontal variability of the diffusivity eddy coefficient plays a crucial role for a correct representation of the mixing processes. Results from experiments with a constant diffusivity coefficient (not shown here) and with a vertically variable but horizontally constant coefficient (EXP1) are qualitatively similar and show the same unsatisfactory aspects, namely: tracers drift, absence of a correct vertical stratification in the Western basin, shallow convection and inadequate mixing properties at the straits.

Some of these model deficiencies are diminished by using any of the three space-dependent tracer diffusivity parameterisations considered in this work. OGCMs typically do not properly resolve the strait morphology and kinematic quantities are strongly constrained by topography: in this situation any parameterisation that automatically increase the eddy diffusivity coefficient in the straits avoids numerical instabilities and improves the physical mixing characteristics. Using the three different space- and time-dependent parameterisations of diffusion we also observed a decrease of the temperature drift, linked with an improvement in the representation of deep convection in the NWM.

We have underlined the necessity of computing the tracer diffusivity coefficient as a function of non-local characteristics of the horizontal velocity field. Observational results from floats velocity spectra and altimeter data justify this idea. The proposed BBRS parameterisation is based on Taylor’s dispersion relation and represents diffusivity processes linked to the time and space variability of the mesoscale generated by the OGCM dynamics. Its main characteristics are the non-locality and the inverse dependence on the square root of enstrophy and the results from the simulations show that these features allow for a better representation of diffusion processes due to large-scale turbulent structures.

In particular, non-locality operates in propagating northward the high-diffusivity characteristics of the north African current and induces in EXP2 and EXP4 a more efficient spreading of the LIW in the North Western basin west of Sardinia channel. On the other hand, the winter deep convection in the area of the Gulf of Lyon with the related meridional overturning cell are better represented in the experiment with BBRS parameterisation (EXP2). In this experiment the convection is still too shallow, but the formed water sinks deeper than LIW and a realistic vertical stratification with a well-defined LIW layer at intermediate depth is reached after  $\sim 100$  years and it is maintained—on time scale longer than the renewal time of the basin—during the rest of the experiment.

The enstrophy factor in BBRS mitigates the dependence of the eddy diffusivity coefficient  $K$  on eddy kinetic energy  $E$  and contributes to lower diffusivity on high-vorticity frontal region, decreasing cross tracer mixing. This mechanism improves the represen-



tation of the tracer’s trapping inside the gyre, leading to a better representation of the dynamical structure in the preconditioning phase of the convection that, in turn, induces a more efficient convection and a better simulation of the overall thermohaline circulation of the Western Mediterranean Sea. Summarising, both the non-locality and the enstrophy dependence in the BBRS parameterisation contribute to make EXP2 the best experiment performed.

The eddy diffusivity parameterisation has to be chosen according to the model peculiarities. In the present case the resolution was sufficient to develop mesoscale features and motivated us for searching diffusivity parameterisations able to take into account the variability generated by the model. We maintained the classical horizontal mixing scheme, because the aim of this work is not to present the “best” numerical representation of diffusion. In a forthcoming paper we will use a simplified model to test the impact of the BBRS parameterisation in the context of the isopycnal mixing and of the Eulerian mean formalism.

The computational effort required by the implementation of the BBRS parameterisation is due to the computation of the averaged Eulerian quantities  $E$  and  $Z$ , and depends on the size of the Eulerian correlation length  $L_E$  of the model. In the present study ( $L_E \sim 150\text{--}200$  km, *i.e.* 7 grid points) this computational effort represents an additional of  $\sim 25\%$  of the total c.p.u. time.

\* \* \*

This work is dedicated to the memory of Dr J. Y. SIMONOT, who first used the BBRS parameterization in his PhD thesis [54], which he defended in 1988, the same year he passed away. This work was supported by the scientific program of the European Science Foundation TAO, by the European project EU MAST III TRACMASS (MAS3-CT97-0142) and by the National Program “Ambiente Mediterraneo” funded by the Italian Ministry for Research and Education (MIUR) and was done using climatologies provided by S. LEVITUS and MODB project partners. We thank R. IACONO for stimulating discussions and A. IACCARINO and E. LOMBARDI for their most valuable work in managing the computers.

## APPENDIX A.

### Model configuration

A standard version of the Cox-Bryan numerical model with rigid-lid approximation [39, 44, 55] is applied to the Mediterranean Sea with realistic coast lines and topography. The horizontal resolution is  $0.25^\circ \times 0.25^\circ$ , while the vertical direction is discretized in 19 levels with thickness varying from 10 m at the surface to 500 m at the bottom. The non-linear UNESCO equation for density is used. The Gibraltar strait is open (two velocity grid points) and the model domain extends in the Atlantic to  $13^\circ$  E, with a buffer zone in the western part (see fig. 1). In the buffer zone temperature and salinity are relaxed on all levels to the Levitus [56] climatology with a time scale of 5 days. Surface salinity is relaxed using a constant 5 days time scale in the Mediterranean domain toward monthly MODB MED5 [42] and in the Atlantic box toward Levitus [56] climatology. To retain the (space) high-frequency variability of the surface forcing we use as surface boundary conditions simultaneous monthly mean values of European Centre Mid-range Weather Forecast (ECMWF) winds and of satellite derived SST of a particular year, iterated perpetually. The surface temperature is then relaxed in the whole domain to monthly mean values of 1988 SST from satellite data [57] using a wind-dependent

relaxation time ( $\gamma$ )<sup>(3)</sup>, while ECMWF monthly mean surface wind fields of 1988 have been used to compute the wind stress and the temperature relaxation time.

The 1988 has been chosen due to the closeness of the SST to climatological values (see, for instance, [58]) in all the basin except in the Adriatic Sea where the 1988 winter SSTs are too warm (*e.g.*, [59]) and a negative bias of about one degree was then added to the local field in February.

Eddy viscosity is assumed to be constant ( $\nu_H = 1.5 \cdot 10^6$  cm<sup>2</sup>/s,  $\nu_V = 1.5$  cm<sup>2</sup>/s) both in time and in space and is represented by a Laplacian operator. Vertical diffusivity is represented by a Laplacian operator with a constant in time vertical profile similar to the profile used by Wu and Haines [46]. To mimic the physics of the mixed layer rather high values (from 3 to 1 cm<sup>2</sup>/s in the first 80 m) are assumed in the upper layers rapidly decreasing to very low values for depths greater than 100 m (0.01 cm<sup>2</sup>/s). With those values of vertical and horizontal diffusivity it can be easily shown that diapycnal mixing due to the horizontal diffusivity is negligible for isopycnal slope smaller than 1/1000 (1/10000) in the upper (lower) layers of the model. Tracer and momentum integration time step is 1 hour. The four experiments of the present work differ only in the representation of the horizontal tracer diffusivity, as described in the text.

## APPENDIX B.

### Algorithm's implementation

B.1. *BRS parameterisation.* – The decorrelation spatial scales, used to define the neighbourhood where one computes the kinematic quantities defining  $K$  (see eq. (5)), are estimated by a preliminary correlation analysis. We consider standard velocity model output on meridional and zonal sections exceeding 30 grid points (*i.e.* for sections longer than  $\sim 750$  km). From the mean velocity correlation function the Eulerian decorrelation length  $L_E$  was estimated by means of the usual first zero crossing technique:

$$L_E = \int_0^\infty R(l) dl \sim \int_0^{l_0} R(l) dl,$$

where  $R(l)$  is the space velocity correlation function and  $l_0$  is the first value in which  $R(l_0) = 0$ . Without entering into details, we found that the zonal component of the velocity field is more correlated than the meridional one that, on the contrary, shows more seasonal variability with a winter maximum (see tables III and IV).

From a time velocity correlation analysis, performed in each grid point by using two days time lagged velocity series, we obtained a mean velocity correlation function for each level. These averaged correlation functions are very smooth and do not show any important depth or seasonal dependence. The first zero cross is after  $\sim 25$ –30 days and the corresponding Eulerian decorrelation time is  $T_E \sim 10$ –15 days. We then define the mean decorrelation scales of the basin equal to  $(L_E, T_E) \sim (100$  km, 10 days).

The averaged values of the eddy kinetic energy  $E$  and enstrophy  $Z$  were then computed for each grid point, in a squared box of  $\sim 175$  km  $\times$  175 km ( $N = 7 \times 7$  grid points) of

---

<sup>(3)</sup> In practice the stronger the wind the smaller is the surface temperature relaxation time that ranges from 2 days to 2 hours for winds exceeding 10 m/s (see [49]). The resulting mean time scale is slightly exceeding one day; small values ( $O(\text{hours})$ ) are confined in the region of the Mistral wind while in the rest of the domain  $\gamma$  assumes rather constant values ( $O(1$ –2 days)).

TABLE III. – *Zonal decorrelation length expressed in km.*

Depth (meters)	Summer	Fall	Winter	Spring	Year
5	121	105	95	111	108
120	115	115	108	114	113
280	110	108	106	112	109
1250	82	86	75	71	79

size comparable to the decorrelation length following

$$E = \frac{1}{N} \sum_{\text{box}} [(u_i - \bar{u})^2 + (v_i - \bar{v})^2],$$

$$Z = \frac{1}{N} \sum_{\text{box}} \left( \frac{\partial}{\partial x} v - \frac{\partial}{\partial y} u \right)^2,$$

where summations and mean mean values ( $\bar{\cdot}$ ) are computed in the squared neighbourhood of the point. This procedure is performed on all the domain each 24 time steps (1 day) and the resulting diffusivity coefficient is computed from

$$(B.1) \quad K = \delta \cdot E \cdot Z^{-1/2},$$

where  $\delta$  is a proportionality constant. The diffusivity field is updated, averaging the 1 day lagged values of  $K$ , every  $\Delta T = 10$  days, *i.e.* with a time lag slightly smaller than  $T_E$ . A space filtering procedure is then applied to the computed  $K(x, y, z, t)$  field. In practice every 10 days we insert in the tracer equation the new space-dependent value of  $K$ . The implementation of the algorithm in the model is easy and consists in adding a Fortran subroutine in the numerical code together with a slight modification of the diffusion algorithm in the tracer equation. The computational effort of the BBRS and Smagorinsky parameterisation is similar and consists in an overhead of  $\sim 25\%$  of the total c.p.u. time.

TABLE IV. – *Meridional decorrelation length expressed in km.*

Depth (meters)	Summer	Fall	Winter	Spring	Year
5	44	47	68	38	49
120	33	33	33	34	33
280	35	35	35	34	35
1250	27	26	21	23	24

## REFERENCES

- [1] ANDREWS D. G., HOLTON J. R. and LEOVY C. B., *Middle Atmosphere Dynamics* (Academic Press) 1987.
- [2] PLUMB R. and MAHLAM J., *J. Atmos. Sci.*, **44** (1987) 298.
- [3] ARMI L., *J. Mar. Res.*, **37** (1979) 515.
- [4] ARMI L. and HAIDVOGEL D. B., *J. Phys. Oceanogr.*, **12** (1982) 785.
- [5] TREGUIER A., HELD I. and LARICHEV V., *J. Phys. Oceanogr.*, **27** (1997) 567.
- [6] VISBECK M., MARSHALL J. and HAINE T., *J. Phys. Oceanogr.*, **27** (1997) 381.
- [7] BRYAN K., DUKOWICZ J. and SMITH R., *J. Phys. Oceanogr.*, **29** (1999) 2442.
- [8] MCWILLIAMS J. and GENT P., *J. Phys. Oceanogr.*, **24** (1994) 46.
- [9] LARICHEV V. and HELD I., *J. Phys. Oceanogr.*, **25** (1995) 2285.
- [10] BABIANO A., BASDEVANT C., LE ROY P. and SADOURNY R., *J. Mar. Res.*, **47** (1987) 107.
- [11] REDI M., *J. Phys. Oceanogr.*, **12** (1982) 1154.
- [12] GENT P. R. and MC WILLIAMS J. C., *J. Phys. Oceanogr.*, **20** (1990) 150.
- [13] TAYLOR G. I., *Proc. London Math. Soc.*, **20** (1921) 196.
- [14] KAMPÉ DE FÉRIET J., *Ann. Soc. Sci. Bruxelles*, **59** (1939) 15.
- [15] BENNET A. F., *J. Atmos. Sci.*, **41** (1984) 1881.
- [16] LARCHEVEQUE M., *Theor. Comput. Fluid Dynamics*, **5** (1993) 212.
- [17] HUA B. L., MC WILLIAMS J. and KLEIN P., *Fluid J. Mech.*, **366** (1998) 87.
- [18] FIGUEROA H. A. and OLSON D. B., *J. Phys. Oceanogr.*, **24** (1994) 371.
- [19] COLIN DE VERDIÈRE, *Mar J. Res.*, **41** (1983) 375.
- [20] KRAUSS W. and BÖNNING C. W., *J. Mar. Res.*, **45** (1987) 252.
- [21] RUPOLO V., HUA B. L., PROVENZALE A. and ARTALE V., *J. Phys. Oceanogr.*, **26** (1996) 1591.
- [22] LUMPKIN R. and FLAMENT P., *J. Mar. Systems*, **24** (2000) 141.
- [23] STAMMER D., *J. Phys. Oceanogr.*, **27** (1997) 1743.
- [24] SMAGORINSKY J., *Mon. Weather Rev.*, **91** (1963) 99.
- [25] NASTROM G. D. and GAGE K. S., *J. Atmos. Sci.*, **42** (1985) 950.
- [26] SMAGORINSKY J., *Some historical remarks on the use of nonlinear viscosities*, in *Large Eddy Simulation of Complex Engineering and Geophysical Flows (Proceeding of an International Workshop in Large Eddy Simulation, Petersburg St., 19-21 Dec. 1990)*, edited by B. GALPERIN and S. A. ORSZAG (Cambridge University Press) 1993, pp. 3-36.
- [27] ROSATI A. and MIYAKODA K., *J. Phys. Oceanogr.*, **18** (1988) 1601.
- [28] MELLOR G. L. and BLUMBERG A. F., *Mon. Weather Rev.*, **113** (1985) 1279.
- [29] HECHT A., PINARDI N. and ROBINSON A. R., *J. Phys. Oceanogr.*, **18** (1988) 1320.
- [30] ROBINSON A. R. and GOLNARAGHI M., *The physical and dynamical oceanography of the Mediterranean Sea*, in *Ocean Processes in Climate Dynamics: Global and Mediterranean Examples*, edited by P. MALANOTTE-RIZZOLI and A. R. ROBINSON (Kluwer Acad., Norwell, Mass.) 1994, pp. 255-306.
- [31] ÖZSOY E., HECHT A., ÜNLÜATA Ü., BRENNER S., SUR H. I., BISHOP J., LATIF M. A., ROZENTRAUB Z. and OGUZ T., *Deep Sea Res.*, Part II, **40** (1993) 1075.
- [32] IUDICONE D., MARULLO S., SANTOLERI R. and GEROSA P., *J. Geophys. Res.*, **103** (1998) 2995.
- [33] HAINES K. and WU P., *J. Mar. Syst.*, **18** (1998) 197.
- [34] MALANOTTE-RIZZOLI P. and HECHT A., *Oceanol. Acta*, **11** (1988) 323.
- [35] ROETHER W., ROUSSENOV V. M. and WELL R., *A tracer study of the thermohaline circulation of the Eastern Mediterranean Sea*, in *Ocean Processes in Climate Dynamics: Global and Mediterranean Examples*, edited by P. MALANOTTE-RIZZOLI and A. R. ROBINSON (Kluwer Acad., Norwell, Mass.) 1994, pp. 239-254.
- [36] MEDOC GROUP, *Nature*, **227** (1970) 1037.

- [37] SCHOTT F., VISBECK M. and SEND U., *Open ocean deep convection, Mediterranean and Greenland seas*, in *Ocean Processes in Climate Dynamics: Global and Mediterranean Examples*, edited by P. MALANOTTE-RIZZOLI and A. R. ROBINSON (Kluwer Acad., Norwell, Mass.) 1994, pp. 203-225.
- [38] MERTENS C. and SCHOTT F., *J. Phys. Oceanogr.*, **28** (1998) 1410.
- [39] WU P. and HAINES K., *J. Geophys. Res.*, **101** (1996) 6591.
- [40] WÜST G., *J. Geophys. Res.*, **66** (1961) 3261.
- [41] MILLOT C., *Oceanol. Acta*, **10** (1987) 143.
- [42] BRASSEUR P., BRANKART J.-M., SCHOENAUEN R. and BECKERS J.-M., *Deep Sea Res.*, **43** (1996) 159.
- [43] MILLOT C., *Dyn. Atmos. Oceans*, **15** (1991) 179.
- [44] ROUSSENOV V., STANEV E., ARTALE V. and PINARDI N., *J. Geophys. Res.*, **100** (1995) 13515.
- [45] CASTELLARI S., PINARDI N. and LEAMAN K., *J. Geophys. Res.*, **105** 10 (2000) 24157.
- [46] WU P. and HAINES K., *J. Geophys. Res.*, **103** (1998) 1121.
- [47] BRYAN K., *J. Comput. Phys.*, **4** (1969) 347.
- [48] COX M. D., *A Primitive Equation, Three Dimensional Model of the Ocean*. GFDL Ocean Group *Tech. Rep. No. 1* (Princeton University, N.J.) 1984.
- [49] ARTALE V., IUDICONE D., SANTOLERI R., RUPOLO V., MARULLO S. and D'ORTENZIO F., *J. Geophys. Res.*, **107**, 10.1029/2000JC00453, August 31, 2002.
- [50] SPARNOCCHIA S., MANZELLA G. M. R. and LA VIOLETTE P. E., *The interannual and seasonal variability of the MAW and LIW core properties in the Western Mediterranean Sea*, in *Seasonal and Interannual Variability of the Western Mediterranean Sea*, edited by P. E. LA VIOLETTE, *Coastal and Estuarine Studies*, Vol. **46** (AGU, Washington) 1994, pp. 177-194.
- [51] ASTRALDI M., GASPARINI G. P. and SPARNOCCHIA S., *The seasonal and interannual variability in the Ligurian-Provencal basin*, in *Seasonal and Interannual Variability of the Western Mediterranean Sea*, edited by P. E. LA VIOLETTE, *Coastal and Estuarine Studies*, Vol. **46** (AGU, Washington) 1994, pp. 93-114.
- [52] BLANKE B. and RAYNAUD S., *J. Phys. Oceanogr.*, **29** (1997) 1038.
- [53] MCWILLIAMS J., *The local dynamics in the western North Atlantic*, in *Eddies in Marine Science*, A. R. Robinson, EWD. (Springer-Verlag) 1983, pp. 92-113.
- [54] SIMONOT J. Y., *Contribution a l'etude des interactions Ocean-Atmospher*, These de doctorat de l'Universite Paris 6 (1988); SIMONOT J. Y., LE TREUT H. and CREPON M., *A Thermodynamic Model of the Global Sea-Surface Temperature and Mixing-Layer Depth, Small-Scale Turbulence and Mixing in the Ocean*, edited by J. C. J. NIHOUL and B. M. JAMART (Elsevier Science Publishers B.V.) 1988.
- [55] PACANOWSKI R. C., DIXON K. and ROSATI A., README file for GFDL MOM1.0 (1990).
- [56] LEVITUS S., *Climatological Atlas of the World Oceans*, NOAA Professional Paper No. 13 (Government U. Printing S. Office, Washington, D.C.) 1982.
- [57] D' F. ORTENZIO, MARULLO S. and SANTOLERI R., *Geophys. Res. Lett.*, **27** (2000) 241.
- [58] MARULLO S., SANTOLERI R., MALANOTTE-RIZZOLI P. and BERGAMASCO A., *J. Mar. Syst.*, **20** (1999) 83.
- [59] GACIC M., MARULLO S., SANTOLERI R. and BERGAMASCO A., *J. Geophys. Res.*, **102** (1997) 22937.